

## A novel method for multi-scale carbon fiber distribution characterization in cement-based composites

Zheng Tong<sup>a</sup>, Haoyan Guo<sup>b</sup>, Jie Gao<sup>c,\*</sup>, Zhenjun Wang<sup>b,d,\*</sup>

<sup>a</sup> Research and Development Center of Transport Industry of Technologies, Materials and Equipments of Highway Construction and Maintenance (Gansu Road & Bridge Construction Group), Lanzhou 730030, Gansu, PR China

<sup>b</sup> School of Materials Science and Engineering, Chang'an University, Xi'an 710061, PR China

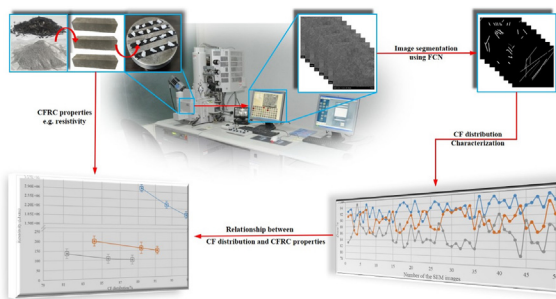
<sup>c</sup> School of Highway, Chang'an University, Xi'an 710064, PR China

<sup>d</sup> Engineering Research Center of Pavement Materials, Ministry of Education of P.R. China, Chang'an University, Xi'an 710061, PR China

### HIGHLIGHTS

- The project presents an application of FCN in characterizing CF distribution in CFRC.
- The FCN-based method computes the CF distribution based on its real distribution.
- The relationship between CF distribution and CFRC properties is analyzed.
- The continuous evaluation method is reasonable for the CF distribution evaluation.

### GRAPHICAL ABSTRACT



### ARTICLE INFO

#### Article history:

Received 2 February 2019

Received in revised form 12 April 2019

Accepted 16 May 2019

Available online 22 May 2019

#### Keywords:

Carbon fiber reinforced cement-based composites

Fully convolutional network

Scanning electron microscope

Carbon fiber distribution

### ABSTRACT

Scanning electron microscope (SEM) is proven effective to analyze the morphology of carbon fibers (CFs) presenting in CFRC. However, the qualitative observation has limited contribution to the improvement of CF distribution as well as the properties of CFRC. In this work, a fully convolutional network (FCN) was developed to segment CFs from SEM images for quantitative CF distribution characterization. Three processes involved in the establishment of the FCN and its application for the CF distribution evaluation, which were: (a) generating a database including 560 CFRC SEM images in different scales; (b) designing, training, and testing an encoder-decoder network and other layers for the FCN; and (c) evaluating the CF distribution and analyzing the relationship between the CF distribution and the CFRC properties using segmentation results. The results showed that the FCN provided reasonable segmentation results for CF clusters with the 0.94F-Measure, 0.92 recall, and 0.96 precision, respectively. The FCN had stable segmentation results under different SEM magnifications. The FCN-based method was proven effective to segment CF clusters in real time, which met the demand for continuous SEM observation. The continuous observation results indicated that the mechanical and electric properties of CFRC were improved by the improvement of the CF distribution.

© 2019 Elsevier Ltd. All rights reserved.

\* Corresponding authors.

E-mail addresses: [highway-gaojie@st.chd.edu.cn](mailto:highway-gaojie@st.chd.edu.cn) (J. Gao), [zjwang@chd.edu.cn](mailto:zjwang@chd.edu.cn) (Z. Wang).

## 1. Introduction

Carbon fiber reinforced cement-based composite (CFRC) has concentrated the intensive studies and been increasingly used as an important engineering material for building and pavement construction. Except for the excellent mechanical performance [1,2], CFRC has many functional properties, including electric heating for pavement deicing [3], electromagnetic wave shielding for buildings [4], and building health monitoring [5,6]. Previous studies have clearly indicated that a good distribution of carbon fibers (CFs) in CFRC is fundamental for achieving functions of CFRC. Generally, three indexes are proven effective in the evaluation of CF distribution morphologies in a CFRC, which are fiber-free area [7], low/high fiber distribution density [8,9] and fiber clusters [10]. Particularly, CF clusters are blamed for the significant deterioration of CFRC in some critical properties, such as bending strength and electrical conductivity. For example, Wang et al. [8] found the distribution of CF and the number of clusters influenced the electrical property of the composites. The study of Gao et al. [11] showed that CFRC had different physical and mechanical properties using different mixing methods owing to the existing of CF clusters. Lu et al. [12] used graphene oxide to modify the distribution and interfacial property of CF clusters to improve the mechanical behavior of CFRC. In summary, the CF distribution in CFRC is critical to properties of CFRC and a high-efficiency detection method for CF clusters and CF distribution can be helpful to improve the CF distribution in CFRC.

A standard approach for fiber distribution evaluation has been introduced in ASTM C1229-94 [13] and CECS38:2004 [14]. In the standard approach, several specimens with equal mass were separated from the fiber reinforce cement paste and then were washed in a square hole sieve with a diameter of 75  $\mu\text{m}$ . The fibers in specimens were collected, dried, and weighted. The fiber distribution was evaluated by the fiber masses. In addition, other theoretical and analytical approaches, such as measurement of electrical resistance [15], microwave heating uniformity [16] and fresh mixture method [17], have been proposed to evaluate fiber distribution. However, these approaches could only analyze CF distribution indirectly but could not characterize the dispersion morphology of CFs. Motivated by the drawback of these traditional approaches, a scanning electron microscope (SEM) approach has been used for the task. For example, Wang et al. [18] and Safiuddin et al. [19] evaluated fracture surface and distribution of CFs in CFRC. However, the evaluation approach using SEM was qualitative and ancillary. Jiang et al. [20] evaluated the thermal conductivity enhancement of phase change materials with carbon fiber network. The SEM images could not reveal the formation of carbon fiber network in its entirety. Additionally, SEM images were utilized to evaluate interfacial strength between CF and cement [21,22], the direct compression strength of single carbon fiber [23], and CF morphology [24,25]. However, the SEM images were just ancillary in these studies. In summary, there were two problems remaining in CF distribution using SEM images: (1) a small observation area in a single SEM image made it impossible to reveal the CF distribution in CFRC in its entirety; (2) complex and no-fixed-form background (objects except for fibers shown in SEM images) and CFs made it difficult to extract CFs from SEM images to evaluate CF distribution quantitatively.

To date, many efforts have devoted to the developments of CF distribution evaluation using SEM images, such as K-value clustering [26], support vector machine [27], and artificial neural network [28]. However, these methods have limitations in both accuracy and efficiency though they are proven effective in some degree. Compared with these conventional methods, convolutional neural

network (CNN) has earned tremendous success in pattern segmentation [29] and various applications [30]. For example, Ming et al. [31] presented an application of a symmetric CNN for mandible segmentation in CT images. The results showed that the proposed symmetric CNN was superior to several methods. Lim et al. [32] utilized CNNs to segment foreground for multiscale feature encoding. The results indicated the performance of the CNN model was reasonable to extract cars, pedestrian, and others from images and videos. Tong et al. [33,34] and Wang et al. [35] employed CNNs to extract asphalt pavement and cement mortar cracks. Performance of the CNNs showed that it had the capacity to handle complex background in the real-world conditions. Liu et al. [36] located carbon powder bundles for the distribution evaluation. The results also indicated CNN models extracted certain objects well from various backgrounds. Therefore, it is possible to utilize CNN or its modified models to extract CFs and CF clusters from SEM images. Generally, CNN has two properties to accomplish the task mentioned above. The first one is automation, which means it is very powerful in extracting low-, mid-, and high-level features from images automatically. This property makes it possible to collect CF cluster features completely without human assistance. The second one is robustness, which means that it has good tolerance of translation and distortion of objects. However, there are still two problems should be solved in the processes to realize the task using CNN: (1) the designed CNN should have the capacity of analyzing SEM images under different scales; (2) the CNN model should segment CFs and CF clusters from SEM images rather than just recognize and locate them in SEM images.

This study presents an application of a fully convolutional network (FCN) to segment CFs from SEM images for the multi-scale cluster detection in CFRC. Then the segmentation results were used to calculate the CF distribution and build a bridge between the microstructures and macro-properties of CFRC. The novelties of this study can be drawn as below:

- The proposed method provides a way to analyze the relationship between the CF distribution and macro-properties of CFRC quantitatively, such as resistivity and bending strength;
- The FCN-based method can be used to compute the CF distribution based on its real distribution in the CFRC rather than the mass of CFs in a specimen;
- The SEM segmentation results can be used for an auxiliary observation in CFRC.

The skeleton of this work is summarized as follows. The research procedures are presented in Section 2, including the processes of collecting SEM images of CFRC, the description of the FCN, and implementation details. The performance of the FCN and its application for the CF distribution evaluation are discussed in Section 3, mainly including the testing performances of the FCN, the continuous segmentation in real time for the CF distribution evaluation, and the relationship analysis between properties of CFRC and the CF distribution. The conclusions of this study are summarized in Section 4.

## 2. Research procedures

### 2.1. Sample preparation and tests

#### 2.1.1. Raw materials

The CFRC composite was fabricated with the Chinese 32.5R Portland cement and PAN-based CF whose density was 1.741 g/ $\text{cm}^3$ , length 3–5 mm, carbon content 94.2%, and diameter 7  $\mu\text{m}$ .

### 2.1.2. Specimen preparation

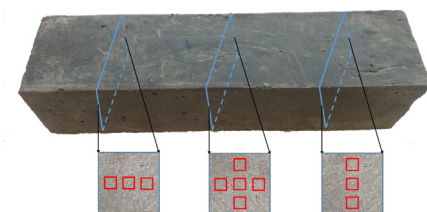
To create the difference of the fiber distribution in specimens, three fiber contents (0.1%, 0.3% and 0.5% of the cement mass) were designed to manufacturing the CFRC specimens. The content of mixing water, sodium carboxymethyl cellulose, and tributyl phosphate were 40%, 0.08%, and 0.016% of cement mass, respectively, and remained the same in all specimens. The mixing processes of the composites, referring to Ref. [37], are shown in Fig. 1. Firstly, the sodium carboxymethyl cellulose was dissolved in the heated mixing water ( $70^{\circ}\text{C}$ ) and stirred for 60 s to create the Mixture 1. Then carbon fibers were mixed with Mixture 1 by a magnetic stirrer. The mixing duration was 120 s, 180 s, or 240 s while the stirring speed was 360 r/m to generate specimens with the same CF mass but different CF distribution. The defoamer was added into Mixture 2 together with the carbon fiber. Afterward, the cement was mixed with Mixture 2 by a cement mortar mixer with 180 s mixing duration. At last, the mixture was poured into a  $40\text{ mm} \times 40\text{ mm} \times 160\text{ mm}$  steel model and vibrated 30 s on a vibration platform. The specimens were placed in a curing room under the temperature  $20 \pm 1^{\circ}\text{C}$  and relative humidity 95%. The specimens are observed by SEM after curing 28 days. In a total of 9 specimens were fabricated (three specimens for each fiber content).

### 2.1.3. SEM image acquisition

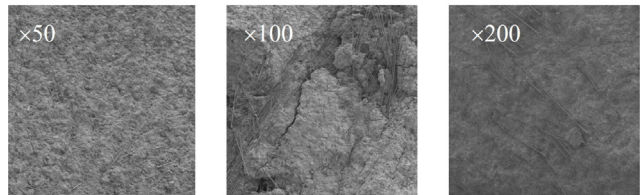
Pu et al. [38] found that the quality of imported images influences the precision of CNN models. In addition, some studies of Ponikiewski et al. [39,40] showed that the high-quality images of CFRC could reflect its distribution precisely. Thus, high-quality SEM images with different scales were collected by a scanning electron microscope in this study to guarantee the integrality of the database. The used technical parameters are 3.5 nm resolutions under high vacuum mode and 2  $\mu\text{A}$  maximum beam. For high-quality SEM images, the samples were coated with gold in a sputter coater.

The dimensions of a full-size CFRC specimen were too large to meet the basic requirement of SEM. Therefore, the observation objects with smaller dimensions, which were suitable for the SEM observation, were selected from the crushed full-size CFRC specimens. Each full-size specimen was crushed by a hand hammer into at least 80 – 100 smaller samples, as such more than 720 samples were obtained from 9 full-size specimens. Fig. 2(a) illustrates examples for selecting observation samples.

During the SEM observation, more than one image was allowed to be captured from the same small-size sample only if images did not overlap in the observation field. To save time, dozens of samples were placed in the sample chamber of the microscope at one time for observation. The SEM observation yield in a total of 560 SEM images, in which there were 240, 200 and 120 SEM images are obtained in 50, 100 and 200 magnifications, respectively. The image size was 1280 pixels  $\times$  1024 pixels. Fig. 2(b) shows some typical SEM images.



(a) Observed samples (The areas in the red boxes are the observed areas)



(b) Example of SEM images

Fig. 2. Observation areas and examples of SEM images.

### 2.1.4. CFRC property tests

To analyze the relationship between the CF distribution and the properties of CFRC, resistivity and bending strength tests were conducted.

A self-designed equipment was used to measure the resistivity of specimens. Two copper sheets with  $38\text{ mm} \times 38\text{ mm} \times 0.5\text{ mm}$  size were used as electrodes. To guarantee the precision of the resistivity measurement, the two sheets were bonded to two sides of a specimen graphite-based epoxy conductive adhesive. One ends of two wires were bonded to the specimen, while other ends were connected with a regulated power supply to conduct conductivity tests. The supply power was 30 V during the measurement. The current values were recorded and used to compute the resistance by Equation (1).

$$\rho = \frac{Rs}{L} \quad (1)$$

where  $\rho$  is the resistivity;  $R$  is the resistance of the specimen;  $s$  is the size of two copper sheets;  $L$  is the length of the specimen.

Bending strength tests were conducted using a material testing system. The distance between anvil tips was 10 cm and the loading rate was 0.05 mm/s. The bending strengths were computed and recorded based on the obtained force–displacement curves.

## 2.2. Fully convolutional networks

### 2.2.1. Fundament works of CNN

Some studies [41,42] showed that image processing for acquired images was also important to analyze the CFRC distribution. In this section, related works of CNN including convolutional layer and pooling layer are introduced briefly. Detailed information of these structural layers has been shown in the Refs. [43,44].

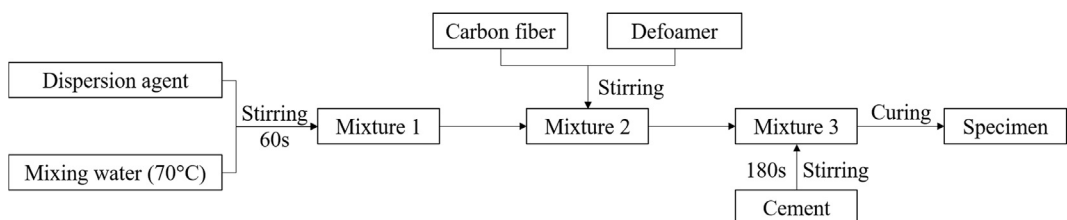


Fig. 1. The processes of preparing CFRC.

Convolutional layer, as the key layer of CNN, is used to extract features by convolution operation using shared-weights kernels. A kernel can be considered as a type of filter, which is a small set of connection weights in neural networks. Generally, a CNN model consists of several convolutional layers with numbers of kernels for extracting different features, such as shapes and grayscales. The operation of convolutional layer can be summed as Eq. (2).

$$z_{\mu,v}^l = \sum_{i=-\infty}^{+\infty} \sum_{j=-\infty}^{+\infty} x_{\mu,v}^{l-1} \cdot k_{rot,ij}^l \cdot \chi(i,j) + b^l \quad (2a)$$

$$\chi(i,j) = \begin{cases} 1, 0 \leq i,j \leq n \\ 0, \text{other} \end{cases} \quad (2b)$$

$$x_{\mu,v}^l = \frac{1}{1 + e^{z_{\mu,v}^{l-1}}} \quad (2c)$$

where,  $x_{\mu,v}^l$  and  $\chi(i,j)$  are the output and input of the element in the  $\mu$ th row and  $v$ th column in the  $l$ th convolutional layer by the convolution operation of a kernel  $k_{ij}^l$ ;  $k_{rot,ij}^l$  is the transposed matrix of a kernel  $k_{ij}^l$ ; and  $b^l$  is the bias in the  $l$ th convolutional layer.

Pooling layer is utilized to decrease the spatial size of its input to reduce the computational costs and the possibility of the overfitting. There are two typical pooling operations, named max pooling and mean pooling. The max pooling as Eq. (3) was adopted in this research.

$$z_{\mu,v}^{l+1} = \max(x_{\mu,v}^l) + b^{l+1} \quad (3a)$$

$$x_{\mu,v}^{l+1} = \frac{1}{1 + e^{z_{\mu,v}^{l+1}}} \quad (3b)$$

### 2.2.2. Encoder-decoder network

A conventional CNN model, whose structure is shown in Fig. 3, can only recognize CFs and CF clusters in the SEM, but cannot define their outer contours. This is because the output of a fully connected layer is the probability of the two objects in the image. For example, the probability of CF is the highest in the probability distribution in Fig. 3. It has clear plausibility that the image in Fig. 3 includes at least a CF. However, the aim of the detection and segmentation of CFs and CF clusters is to acquire the areas of the two objects in SEM images to analyze the CF distribution. Therefore, an encoder-decoder network was developed to modify the traditional CNN in this work.

In the modified CNN with an encoder-decoder network, fully connected layers were replaced by deconvolutional layers. The modified CNN was named fully convolutional network (FCN). The structure and parameters of the FCN are shown in Fig. 4. The FCN could be divided into two parts. The first part was the same as a conventional CNN including convolutional layers and pooling lay-

ers. The function of this part was to extract features of CFs and clusters from SEM images. In other words, it was an operation for encoding SEM images. Thus, this part was named “encoder”. The output of the encoder was a dense probability mask with large depth. The depth of dense probability mask in our research was 4096. A dense probability mask was also regarded as extracted features. As shown in Fig. 4, the output of the encoder was fed to the second part. The extracted features were used for upsampling operation in the second part. The function of the second part was to perform the deconvolution to produce segmentation results. In other words, it was an operation for decoding extracted features to acquire segmentation results. Thus, this part was named “decoder”. To improve computational efficiency and non-linearity of the segmentation function, upsampling was used in each layer of the decoder. Therefore, the function layers for “encoder” and “decoder” were summed as an encoder-decoder network.

In contrast to traditional CNN, the upsampling operation was used to product segmentation results in the FCN. Processes of upsampling were also called deconvolution or transposed convolution. It could be summarized as Eq. (4),

$$y_{u+1}^i = \sum_{k=1}^K z_{u,k}^i \oplus f_{k,c}^u \quad (4)$$

where,  $y_{u+1}^i$  and  $z_{u,k}^i$  were the output and input of  $u$ th upsampling layer, respectively.  $K$  and  $c$  were the numbers of kernels and feature maps in the  $u$ th upsampling layer.  $f$  stood as a weight matrix of kernels in the  $u$ th upsampling layer.  $\oplus$  stands as a deconvolutional operation. An example of a transposed convolution is shown in Fig. 5. The input size of the example matrix is  $2 \times 2$ . The size of the transposed convolution kernel is  $3 \times 3$ . The transposed convolution kernel slides the input matrix from the left-upper corner to the lower-right corner to make dot products. A  $4 \times 4$  matrix is acquired after the operation. Assuming the input depth of the example matrix is 4096, the output depth of the example matrix turns to 2048 after a transposed convolution. Similarly, the  $3 \times 3$ ,  $5 \times 5$ ,  $7 \times 7$ ,  $9 \times 9$ , and  $11 \times 11$  transposed convolution kernels were also utilized in the decoder in Fig. 4 to turn extract features of CFs and clusters to a segmentation result. Thus, a segmentation result had the same size as the input image but only areas of CFs and CF clusters are reserved in the segmentation image.

### 2.3. Implementation details and database

The FCN was used to segment areas of CFs and CF clusters from SEM images. The function mentioned above was realized by training the FCN. During the training, the labels of SEM images were the ground-truth areas of CFs and CF clusters in SEM images. The aim of the training was to minimize the errors between the output areas of CFs and CF clusters and the ground-truth areas. The errors were computed using an average binary cross entropy loss for each

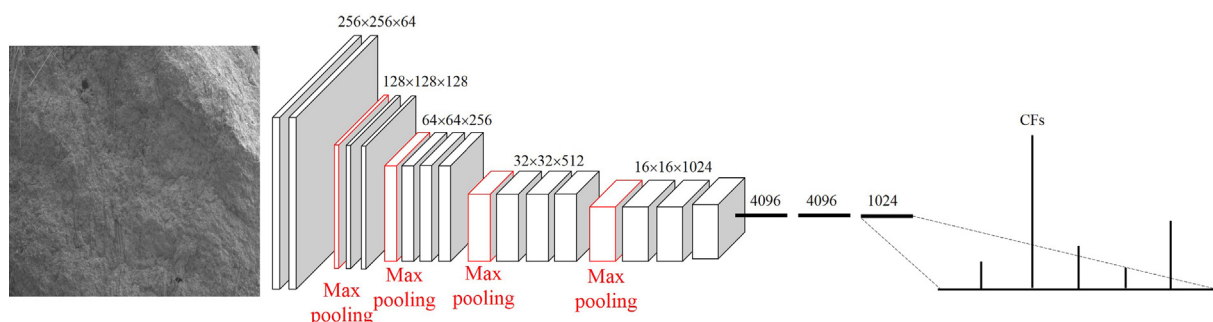
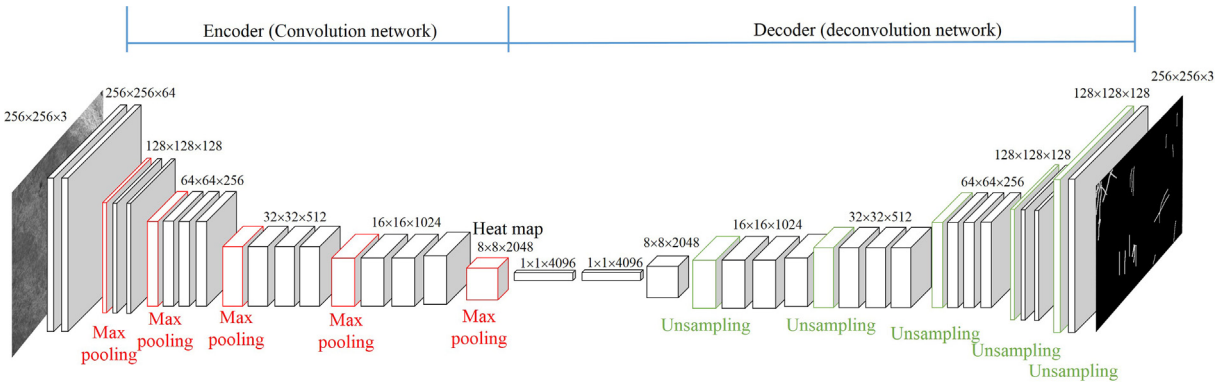
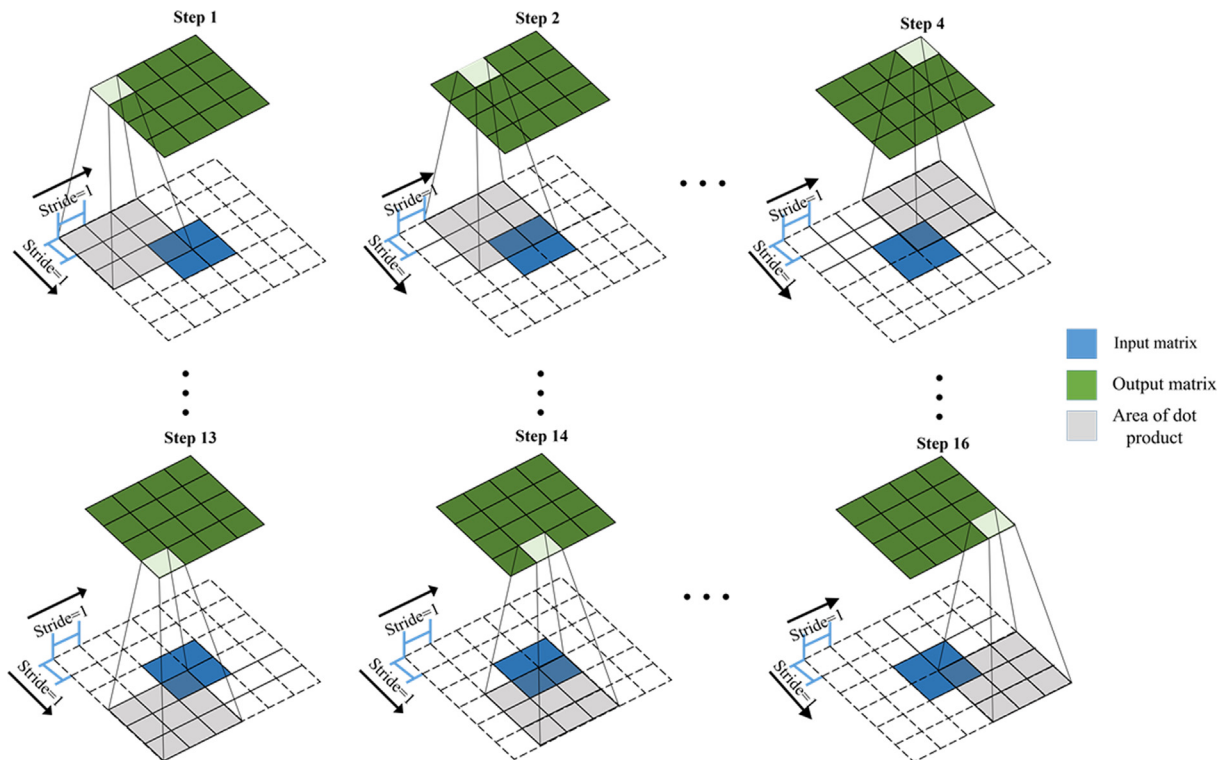


Fig. 3. Structure of a traditional convolutional neural network.



**Fig. 4.** Structure of fully convolutional network.



**Fig. 5.** Example of upsampling.

pixel in an image by Eq. (5). Thus, the gradients of the error were computed by Eq. (6).

$$\text{error} = - \sum_{i=1}^n y'_i \log f(z_i) \quad (5a)$$

$$f(z_k) = \frac{e^{z_k-m}}{\sum_{i=1}^n e^{z_i-m}} \quad (5b)$$

$$\frac{\partial \text{error}}{\partial z_i} = \begin{cases} f(z_i) - 1 & i = k \\ f(z_i) & i \neq k \end{cases} \quad (6)$$

where,  $y'_i$  was the ground truth of an image;  $k$  was the number of the labeled neural units;  $n$  stood the total element number of the outputs;  $m$  was the maximum element of the output. The batch size for training the FCN was 1.

The learning rate was 1e-4 in our research to guarantee that the weights of convolution and deconvolution kernels were not adjusted sharply. The max 50 epochs for 200 training samples was set to prevent overfitting. During the training, a model checkpoint was utilized to save the best model when validation loss decreased.

The database for training, validation, and testing was another key to accomplish the segmentation. Totally, 560 SEM images with 1280 pixels  $\times$  1024 pixels were generated. These images were cropped into small images with 256 pixels  $\times$  256 pixels to respond to the size of the input layer. A part of cropped images with no CFs and clusters were deleted, and 8356 cropped images were acquired and used to generate a database. The 4557 and 1520 cropped images were selected randomly as the training set and validation set. The rest cropped images were used as the testing set. All the training, validation, and testing sets included images in three con-

ditions: (1) there was no CF and cluster; (2) there were CFs but no cluster; (3) there was one cluster or more.

### 3. Results and discussion

#### 3.1. Testing performance

Four indexes were used to evaluate the overall performance of the trained FCN, including recall, precision, percentage of wrong classifications (PWC), and F-Measure. In the task of CF and cluster segmentation, the true positive (TP) was the true number of CFs and clusters, while the true negative (TN) was the true number of backgrounds. Additionally, the false positive (FP) was the wrong number of CFs and cluster, while the false negative (FN) was the wrong number of backgrounds. Thus, recall, precision, PWC, and F-Measure were computed by Eqs. (7)–(10), respectively.

$$\text{Recall} = \frac{\text{TP}}{\text{TP} + \text{FN}} \quad (7)$$

$$\text{Precision} = \frac{\text{TP}}{\text{TP} + \text{FP}} \quad (8)$$

$$\text{PWC} = \frac{\text{FN} + \text{FP}}{\text{TN} + \text{TP} + \text{FN} + \text{FP}} \quad (9)$$

$$\text{F - Measure} = \frac{2 \times \text{Precision} \times \text{Recall}}{\text{Precision} + \text{Recall}} \quad (10)$$

The overall performance of the testing is shown in Table 1. Each row shows the average results of each category. The last row shows the average results across 2 categories. Only the testing data set was utilized in the reported performance. The FCN generated an overall F-Measure of 0.9403 in the testing. It indicated the trained FCN had a high accuracy in the segmentation task. The FCN had a higher average F-Measure in the CF segmentation than in the cluster segmentation. Thus, the FCN had better performance in segmenting dispersive CFs, though the average F-Measure of cluster segmentation was also acceptable. The average precisions of CF and cluster segmentation were 0.9672 and 0.9597, which were similar. However, the recall of clusters was lower than the recall of CF. Therefore, a further evaluation with a new index was conducted for to verify whether the FP of the FCN in the cluster segmentation was acceptable or not.

Dice similarity coefficient (DSC) was used to further evaluate the CF segmentation performance of the FCN. As the most popular evaluation criterion [45], DSC was defined in Eq. (11). In the following equation,  $Y_i$  is the output of FCN in the  $i^{\text{th}}$  pixel, while  $T_i$  is the ground truth in the  $i^{\text{th}}$  pixel.

$$\text{DSC} = \frac{1}{n} \sum_{i=1}^n \frac{2(|Y_i \cap T_i|)}{|Y_i| + |T_i|} \quad (11)$$

Fig. 6 presents the DSC evaluation on the FCN using 15 testing samples with CF clusters. The DSC curves of the 15 testing samples were stable when the recall was in the range of 0.1–0.9. It indicated that the FCN had the robust performance in the testing samples even the recall in Table 2 was not perfect. The 15 testing samples and their segmentation result are shown in Fig. 7. It showed that

the FCN distinguished the CF cluster with the background, such as hydration products and voids, though a small number of CFs in the CF cluster were lost. The loss of the small number of CFs in the CF clusters led the low recall. However, it did not influence the overall segmentation of the CF clusters because the profile of a CF cluster in segmentation result was obviously different from the profile of a single CF. Additionally, as shown in the right parts of Fig. 7 (No. 1), the trained FCN distinguished CFs from grooves, which were led by the dissociation of CFs during the observation. The grayscales and shapes of grooves are close to the CFs. This distinguishing capacity showed that the trained FCN could even classify objects, whose features could not be defined easily.

The overall performance cannot reflect the segmentation capacity of the FCN on different scales. Considering the aim of the FCN was multi-scale cluster detection, a stability study of the segmentation performance on different magnifications was conducted. The database included three magnifications,  $\times 50$ ,  $\times 100$ ,  $\times 200$ . The testing set was divided based under the magnifications. The overall performance of testing under different magnifications is shown in Table 2.

The FCN generated average F-Measures of 0.9498, 0.9434, and 0.9291 under  $\times 50$ ,  $\times 100$ , and  $\times 200$  magnifications, respectively. It indicated that the performances of the FCN under different magnifications were similar, though the performances of the FCN under  $\times 50$  and  $\times 100$  to segment CFs is slightly better than the performance of the FCN under  $\times 200$ . The reason why the FCN could segment CFs and CF clusters from complex background under different magnifications was mainly that the shapes of CFs under different magnifications were similar in the SEM images. For example, two testing samples, shown in Fig. 8(a) and Fig. 8(b), were under  $\times 50$  and  $\times 200$  magnifications, respectively. The segmentation results are shown in Fig. 8(c) and Fig. 8(d). The segmentation results of the two samples were both acceptable. The visualizations of the feature maps are shown in Fig. 8(e)–(j). Fig. 8(e)–(g) are the visualizations of the feature maps of the testing samples under  $\times 50$  magnifications, while Fig. 8(h)–(j) are the visualization of the feature maps of the testing samples under  $\times 200$  magnifications. All feature maps in Fig. 8 were randomly chosen from each layer of the FCN and scaled to the same size. Fig. 8(e)–(j) illustrated that the FCN had the capacity for extracting features of SEM images, such as outlines and changes of grayscales, regardless of magnifications. The reasons why the FCN could extract features with different types was that the kernels in different convolution layers could extract different features though SEM images under different magnifications showed different features of CFs, clusters, and voids. For example, a part of the kernel visualizations in the first convolution layer shown in Fig. 9. The kernels shown in Fig. 9 I1–I18 can extract different shapes. The kernels shown in Fig. 9 III1–III8 can extract different grayscale changes, while the kernels shown in Fig. 9 IV1–IV8 can extract different grayscales. Additionally, it also because the pooling operation in encoder increased FCN's tolerance of distortion and scaling.

#### 3.2. Continuous segmentation in real time for CF distribution evaluation

The study of Chung et al. [46] proved that the use of SEM to assess material characteristics is ineffective because of the small observation area in a SEM image for the whole sample. Therefore, a continuous segmentation and observation in real time were necessary to add observation areas to realize the CF distribution evaluation using SEM. For example, the observation area of a SEM image under  $\times 50$  magnification was  $0.5 \text{ mm} \times 0.5 \text{ mm}$ . A  $25 \text{ mm} \times 25 \text{ mm}$  area could be observed and its CF distribution could be analyzed once 50 continuous SEM images without overlap were segmented in real time by the FCN, which was enough for the

**Table 1**  
Testing results.

Category	Recall	Precision	PWC	F-Measure
CF	0.9486	0.9672	0.1180	0.9578
CF cluster	0.8817	0.9597	0.2694	0.9190
Overall	0.9281	0.9645	0.1069	0.9403

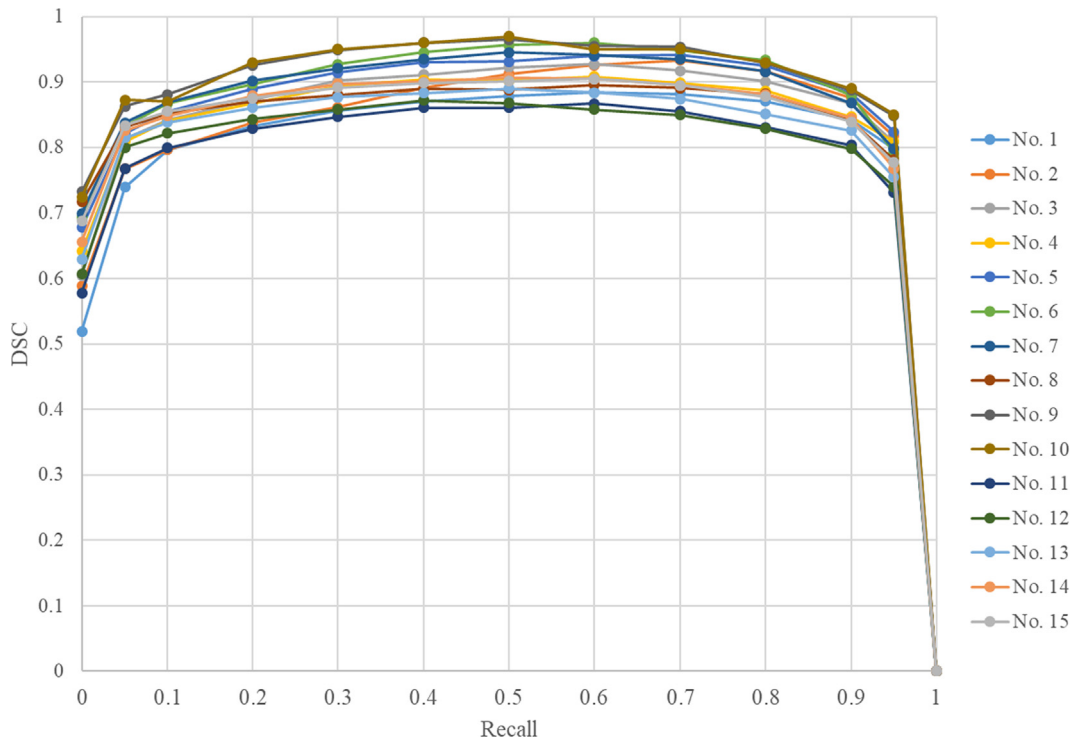


**Fig. 6.** Results of FCN on 15 testing samples.

**Table 2**  
Testing results under different magnifications.

Category	$\times 50$				$\times 100$				$\times 200$			
	R	P	PWC	F-M	R	P	PWC	F-M	R	P	PWC	F-M
CF	0.9468	0.9805	0.1392	0.9634	0.9350	0.9779	0.0523	0.9560	0.9670	0.9501	0.1475	0.9585
CF clusters	0.9038	0.9710	0.0736	0.9362	0.8936	0.9714	0.0759	0.9309	0.8374	0.9718	0.0732	0.8996
Overall	0.9253	0.9758	0.1064	0.9498	0.9143	0.9747	0.0641	0.9434	0.9022	0.9610	0.1103	0.9291

Note: R, P, and FM denote Recall, Precision, and F-Measure.

CF distribution evaluation for the whole sample. In this study, Equation (12) and Equation (13) were used to calculate the CF distribution in a SEM image and an observation area, respectively.

$$D_{SEM} = \frac{A_{No\ CF} + A_{Single\ CF}}{A_{No\ CF} + A_{CF\ clusters} + A_{Single\ CF}} \quad (12)$$

$$D_{Sample} = \frac{1}{n} \sum_{i=1}^n D_{SEM,i} \quad (13)$$

where  $D_{SEM}$  and  $D_{Sample}$  are CF distribution in a SEM image and a sample, respectively.  $A_{CF}$  clusters,  $A_{No\ CF}$ , and  $A_{Single\ CF}$  are the areas of CF clusters, background, and single CFs in a SEM image.

The testing results showed that the average runtime of the FCN in GPU mode to process one SEM image with 1280 pixels  $\times$  1024 pixels was 0.17 s/image. It illustrated that five SEM images could be segmented by the FCN in a second approximately. The segmentation speed met the demand for SEM observation in real time in theory. Figs. 10 and 11 presents observation areas in 3 s and their segmentation results by the FCN, respectively. The processes were accomplished in real time, which indicated the real-time segmentation as an auxiliary observation in the SEM was feasible.

Fig. 12 present the continuous evaluation results of the CF distribution in the specimens with three fiber contents (0.1%, 0.3% and 0.5% of the cement mass) and 180 s mixing time under  $\times 50$  magnification. The results of  $D_{SEM}$  in each specimen varied from one

to another. It indicated that the  $D_{SEM}$  was not effective to evaluate the CF distribution. The results of  $D_{sample}$  became stable with the increase of the observation areas. For example, the  $D_{sample}$  in the 0.3% fiber contents specimen for the first 40 and the 50 SEM images were 89.38% and 89.36%. Additionally, the results of the  $D_{sample}$  using 50 SEM in the three specimens were 92.29%, 89.36%, and 85.62%, respectively. The results were close to the real results. It indicated that the continuous evaluation method based on  $D_{sample}$  was reasonable for the CF distribution evaluation in the CFRC specimen, which overcame the disadvantage of the small observation areas in a SEM image.

In summary, the processes for the proposed approach in this study for CF distribution could be drawn as below:

- (1) Several specimens were separated from the CFRC;
- (2) Continuous observation and collection of SEM images from these specimens were conducted. In general, 50 images without overlapping should be collected from the CFRC;
- (3) Continuous segmentation results were generated using the FCN and used to calculated  $D_{sample}$  as the CF distribution.

### 3.3. Relationship between properties of CFRC and the CF distribution

The previous studies showed that the CF distribution had a striking effect on the properties of the CFRC specimens,

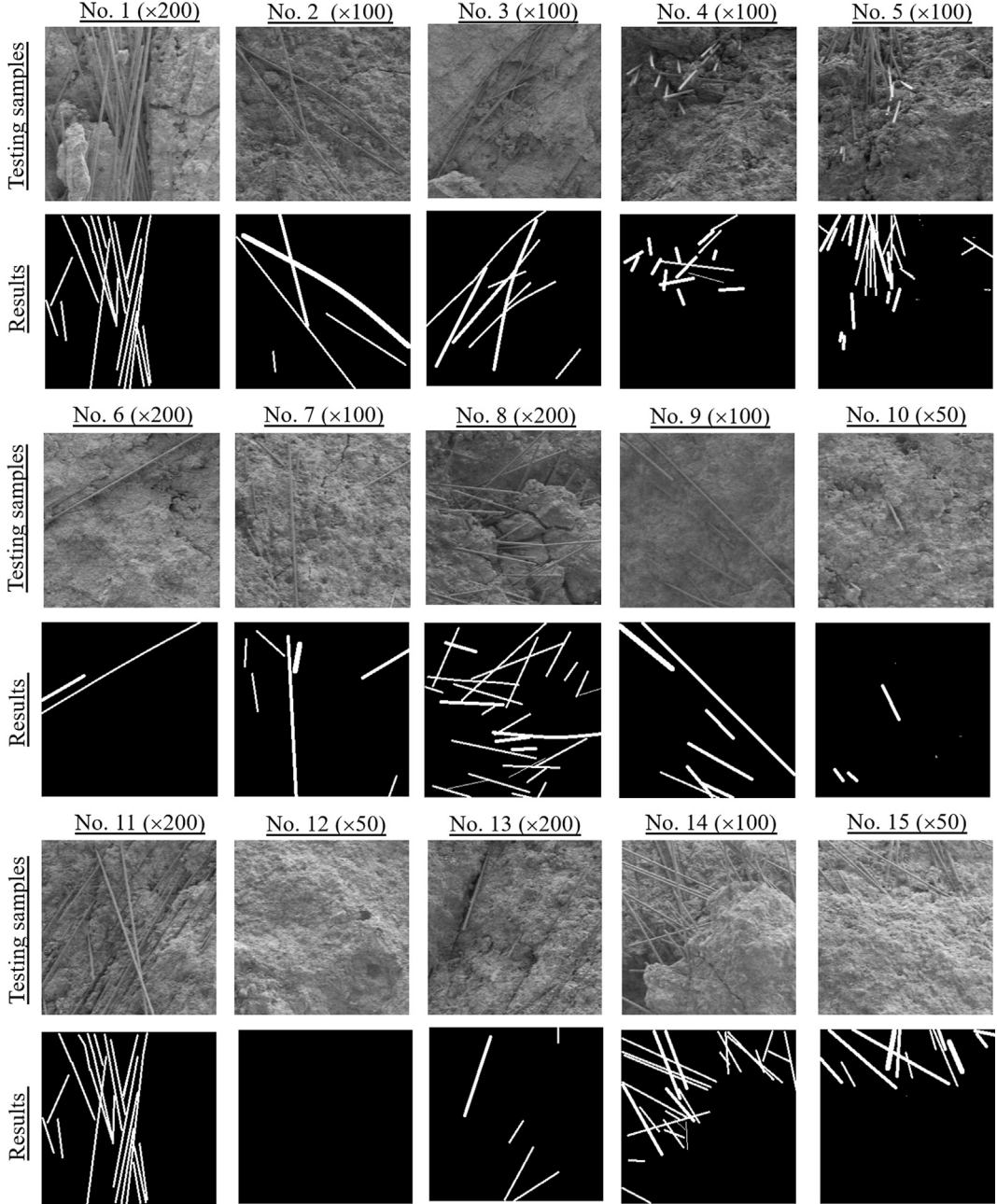


**Fig. 7.** Testing samples and segmentation results.

e.g. mechanical property [2] and electric heating property [3]. However, these studies only used the mass fraction of CFs to characterize the CF distribution due to the limitation of the observation areas of the SEM. It was feasible to analyze the relationship between the properties of CFRC and the CF distribution once the CF distribution was calculated based on the microscopic structure of CFRC.

### 3.3.1. Resistivity

The resistivity is an indispensable property of CFRC, which is related to its electric heating rate and microwave absorption. However, the CFRCs with the same CF mass might have different CF distribution, which led to different resistivities. Thus, it was necessary to investigate the relationship between the CF distribution and resistivity of the CFRC. Thus, the resistivity tests were conducted to explain the relationship between the CF distribution and the resistivity of CFRCs.

**Fig. 13** presents the resistivity results of specimens with different carbon fiber distribution (three fiber contents and three mixing times). A sharp decline of the resistivity is shown in **Fig. 13** with the increase of the CF distribution. It indicated that the good CF distribution had a positive effect on the improvement of the conductivity of CFRC, though its effect was less than the effect of the CF masses. Therefore, the electric properties of the CFRC could be modified by the reasonable mixing methods. Additionally, as shown in **Fig. 13**, it was important to guarantee  $D_{sample}$  larger than 85% to ensure the conductivity of the CFRC when the range of the CF mass was in 0.1–0.5%.

### 3.3.2. Mechanical property

The mechanical properties of CFRC have been intensively investigated in previous studies [47,48]. However, these studies only presented correlations between the CF masses and mechanical properties because they could not utilize the SEM images to

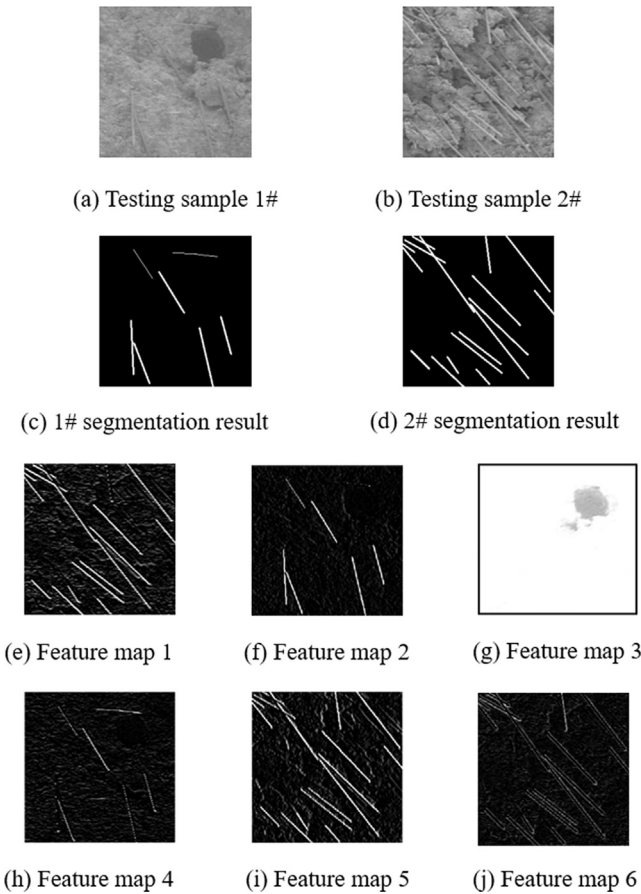


**Fig. 8.** Two testing samples, their segmentation results of the FCN, and visualization on the feature map of the FCN.

calculate the CF distribution quantificationally. However, the CFRCs with the same CF mass might have different CF distribution, which led to different mechanical properties. Thus, it was necessary to investigate the relationship between the CF distribution and mechanical properties of the CFRC.

Fig. 14 presents the bending strength results of specimens with different carbon fiber distribution (three fiber contents and three mixing times). The bending strength increased with the improvement of the CF distribution. It indicated that the incorporation of

CFs with reasonable mixing methods could significantly improve the bending strength of the hardened cement paste. Thus, it was essential to focus not only on the mass but also the distribution of CFs to improve the mechanical properties of CFRC. Additionally, as shown in Fig. 14, it was important to guarantee  $D_{sample}$  larger than 87% to ensure the bending strength of the CFRC when the range of the CF mass was in 0.1–0.5%.

The results present in Figs. 13 and 14 proved that the FCN-based method for the CF distribution evaluation provided a way to build a bridge between the microstructures and macro-properties of CFRC, not only limited to the resistivity and bending strength. Thus, this work proved a desirable preliminary study of building the relationship between the CF distribution and the properties of CFRC. In the further study, more specimens with different CF distribution should be observed by the SEM and measured by different property tests to build a correction between the microstructures and macro-properties of CFRC.

#### 4. Conclusions

An application of the CF segmentation and distribution evaluation using FCN and SEM images was presented in this work and the following conclusions can be drawn:

- (1) The FCN-based method provided a way to build a bridge between the CF distribution and macro-properties of CFRC. The CF distribution was computed using continuous segmentation results of SEM images. It could reflect the real CF distribution in the CFRC rather than the mass of CFs in a specimen.
- (2) The FCN was used for CF cluster segmentation, achieving an average F-Measure of 0.9403, recall of 0.9281, and precision of 0.9645. The DSC curves of the FCN were stable. The average F-Measures was 0.9498, 0.9434, and 0.9291 under  $\times 50$ ,  $\times 100$ , and  $\times 200$  magnifications, respectively. These indicated that the FCN could be considered as the reasonable model with acceptable stability in this work.
- (3) The results of DSEM varied from one to another. It indicated that the DSEM was not effective to evaluate the CF distribution. With the increase of the observation areas, the results of  $D_{sample}$  became stable and close to the real results. It indicated that the continuous evaluation method based on  $D_{sample}$  was reasonable for the CF distribution evaluation in the CFRC specimen, which overcome the disadvantage of the small observation areas in a SEM image.

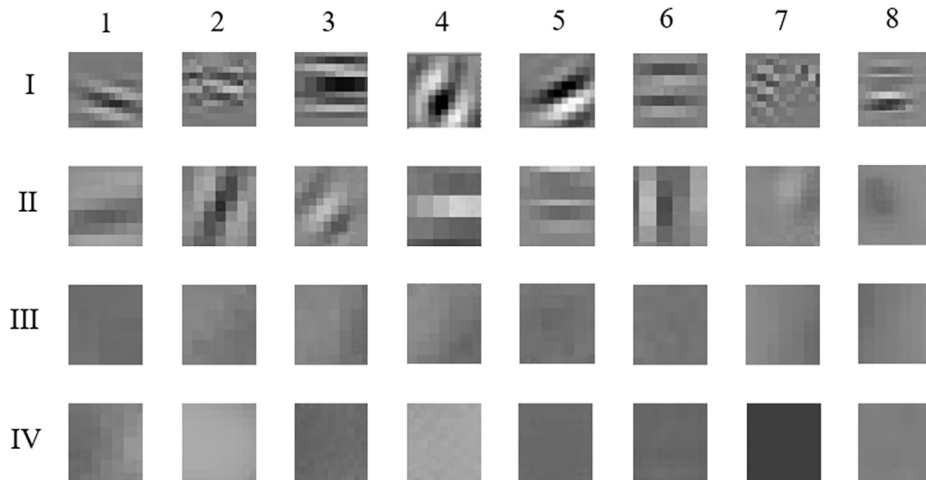


**Fig. 9.** Visualization on the kernels.

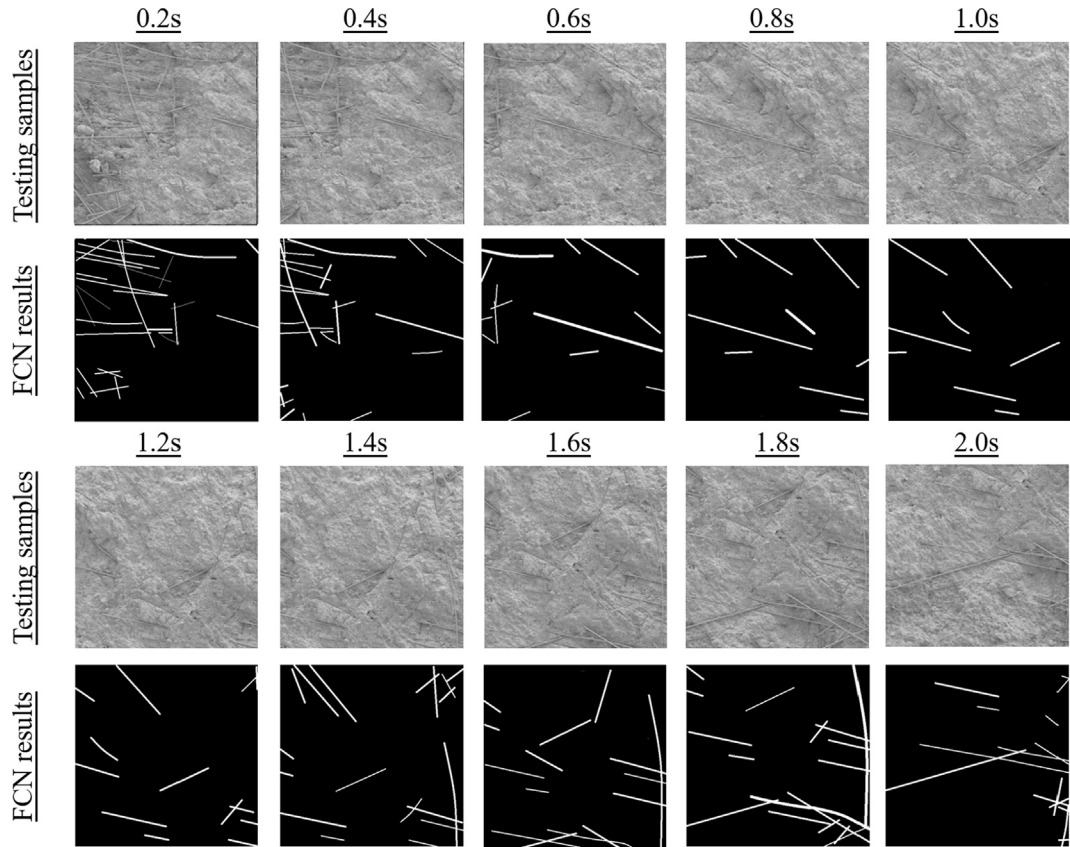


**Fig. 10.** The first real-time observation areas and segmentation results ( $\times 50$ ).

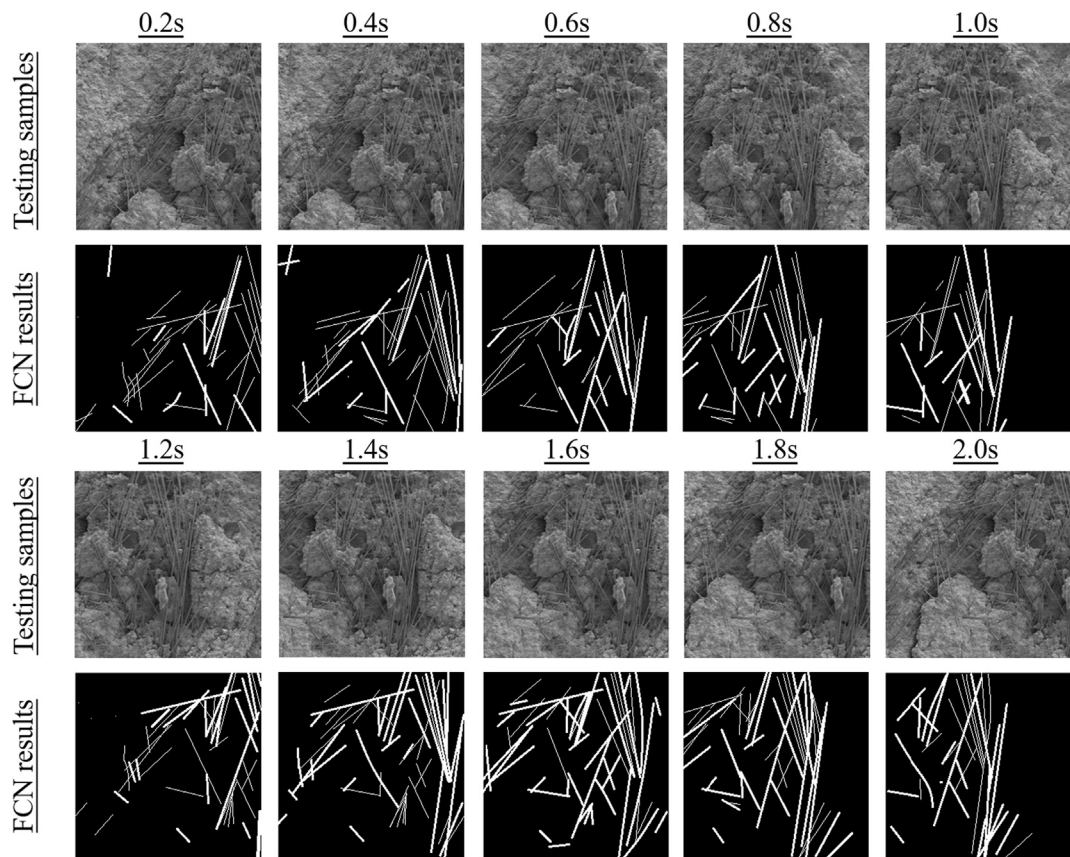


**Fig. 11.** The second real-time observation areas and segmentation results ( $\times 100$ ).

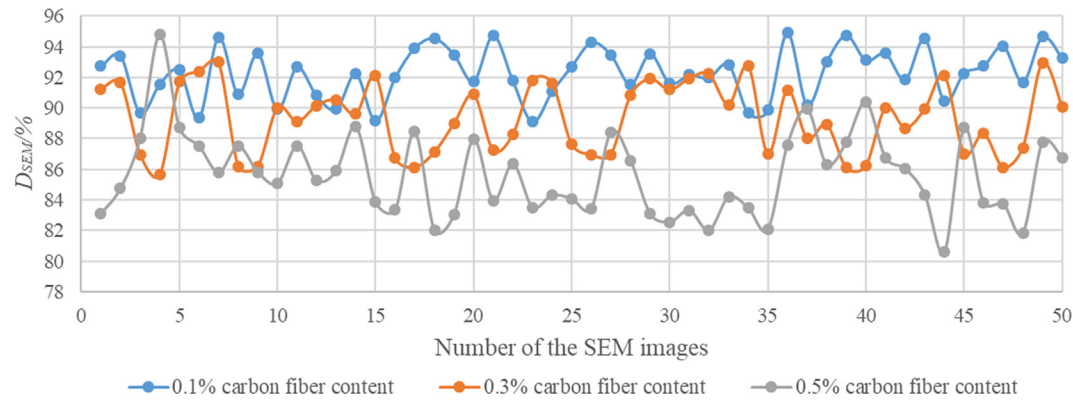
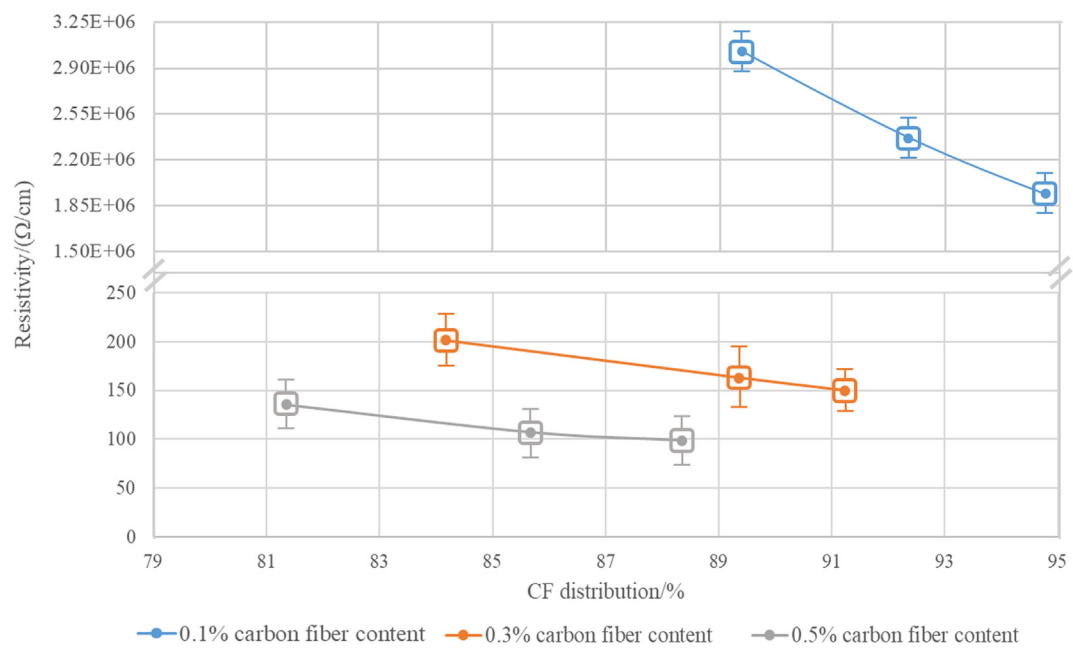
Fig. 12. Continuous evaluation results of the CF under  $\times 50$  magnification.

Fig. 13. Resistivity of specimens with different carbon fiber distribution.

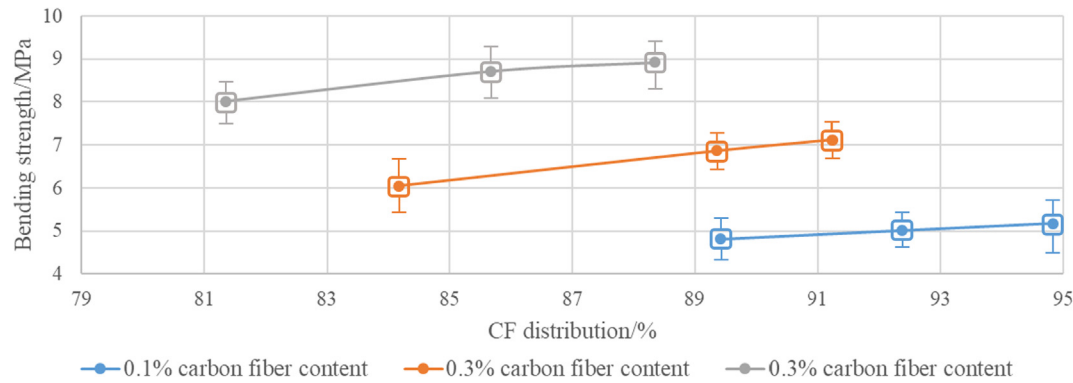


Fig. 14. Bending strength of specimens with different carbon fiber distribution.

- (4) The resistivity of CFRC decreased sharply with the increase of the CF distribution. It indicated that the good CF distribution had a positive effect on the improvement of the conductivity

CFRC. It was important to guarantee  $D_{\text{sample}}$  larger than 85% to ensure the conductivity of the CFRC when the range of the CF mass was in 0.1–0.5%.

(5) The bending strength increased with the improvement of the CF distribution. It indicated that the incorporation of CFs with reasonable mixing methods could significantly improve the bending strength of the hardened cement paste. It was important to guarantee  $D_{sample}$  larger than 87% to ensure the bending strength of the CFRC when the range of the CF mass was in 0.1–0.5%.

## Declaration of Competing Interest

None.

## Acknowledgements

The authors gratefully acknowledge the financial support provided by Opening Foundation of Research and Development Center of Transport Industry of Technologies, Materials and Equipments of Highway Construction and Maintenance. (Gansu Road & Bridge Construction Group) (No. GLKF201811). This work was also supported by the China-UK Research and Innovation Partnership Fund (Newton Fund) jointly funded by the China Scholarship Council and British Council; the State Key Laboratory of High Performance Civil Engineering Materials (No. 2018CEM010); the Fundamental Research Funds for the Central Universities of China (Nos. 300102318402, 300102219509 and 300102319501) and Co-operation Program with the UTs and INSAs (France) funded by the China Scholarship Council (No. CSC201801810108).

## References

- [1] Wenjie Wang, Nawawi Chouw, Flexural behaviour of FFRP wrapped CFRC beams under static and impact loadings, *Int. J. Impact Eng.* 111 (2018) 46–54.
- [2] Khiem Quang Tran, Tomoaki Satomi, Hiroshi Takahashi, Improvement of mechanical behavior of cemented soil reinforced with waste cornsilk fibers, *Constr. Build. Mater.* 178 (2018) 204–210.
- [3] Ziyi Wang, Zhi Wang, Mei Ning, Shengxuan Tang, Yunfei He, Electro-thermal properties and Seebeck effect of conductive mortar and its use in self-heating and self-sensing system, *Ceram. Int.* 43 (12) (2017) 8685–8693.
- [4] Chuang Wang, Kezhi Li, Hejun Li, Lingjun Guo, Gengsheng Jiao, Influence of CVI treatment of carbon fibers on the electromagnetic interference of CFRC composites, *Cem. Concr. Compos.* 30 (6) (2008) 478–485.
- [5] Manuela Chiarello, Raffaele Zinno, Electrical conductivity of self-monitoring CFRC, *Cem. Concr. Compos.* 27 (4) (2005) 463–469.
- [6] Faezeh Azhari, Nemkumar Banthia, Cement-based sensors with carbon fibers and carbon nanotubes for piezoresistive sensing, *Cem. Concr. Compos.* 34 (7) (2012) 866–873.
- [7] Guofeng Qin, Jingxin Na, Mu. Wenlong, Wei Tan, Jiazhong Yang, Junming Ren, Effect of continuous high temperature exposure on the adhesive strength of epoxy adhesive, CFRP and adhesively bonded CFRP-aluminum alloy joints, *Compos. B Eng.* 154 (2018) 43–55.
- [8] Wang Chuang, Jiao Geng-sheng, Li Bing-liang, Peng Lei, Feng Ying, Gao Ni, Li Ke-zhi, Distribution of carbon fibers and conductivity of carbon fiber-reinforced cement-based composites, *Ceram. Int.* 43 (17) (2017) 15122–15132.
- [9] Young-Jae Lee, Hyek-Jong Joo, Ljubisa R. Radovic, Preferential distribution and oxidation inhibiting/catalytic effects of boron in carbon fiber reinforced carbon (CFRC) composites, *Carbon* 41 (13) (2003) 2591–2600.
- [10] Wang Chuang, Peng Lei, Li Bing-liang, Gao Ni, Zhao Li-ping, Li Ke-zhi, Influences of molding processes and different dispersants on the distribution of chopped carbon fibers in cement matrix, *Helyion* 4 (10) (2018) e00868.
- [11] Jie Gao, Zhenjun Wang, Ting Zhang, Liang Zhou, Distribution of carbon fibers in cement-based composites with different mixing methods, *Constr. Build. Mater.* 134 (2017) 220–227.
- [12] Zeyu Lu, Asad Hanif, Guoxing Sun, Rui Liang, Pavithra Parthasarathy, Zongjin Li, Highly dispersed graphene oxide electrodeposited carbon fiber reinforced cement-based materials with enhanced mechanical properties, *Cem. Concr. Compos.* 87 (2018) 220–228.
- [13] CECS38:2004Technical Specification for Fiber Reinforced Concrete Structures, General Administration of Quality Supervision, Inspection and Quarantine of the People's Republic of China, Beijing, 2004.
- [14] ASTM C1229-94Standard Test Method for Determination of Glass Fiber Content in Glass Fiber Reinforced Concrete (GFRC) (Wash-Out Test), ASTM International, West Conshohocken, PA, 2015.
- [15] Carlos G. Berrocal, Karla Hornbostel, Mette R. Geiker, Ingemar Löfgren, Karin Lundgren, Dimitrios G. Bekas, Electrical resistivity measurements in steel fibre reinforced cementitious materials, *Cem. Concr. Compos.* 89 (2018) 216–229.
- [16] Jie Gao, Haoyan Guo, Xiaofeng Wang, Pei Wang, Yongfeng Wei, Zhenjun Wang, Yue Huang, Bo Yang, Microwave deicing for asphalt mixture containing steel wool fibers, *J. Cleaner Prod.* 206 (2019) 1110–1122.
- [17] Yuanxia Yang, Methods study on dispersion of fibers in CFRC, *Cem. Concr. Res.* 32 (5) (2002) 747–750.
- [18] Wang Chuang, Jiao Geng-sheng, Li Bing-liang, Peng Lei, Feng Ying, Gao Ni, Li Ke-zhi, Dispersion of carbon fibers and conductivity of carbon fiber-reinforced cement-based composites, *Ceram. Int.* 43 (17) (2017) 15122–15132.
- [19] Md. Sufiuddin, M. Yakhlef, K.A. Soudki, Key mechanical properties and microstructure of carbon fibre reinforced self-consolidating concrete, *Constr. Build. Mater.* 164 (2018) 477–488.
- [20] Zhao Jiang, Ting Ouyang, Yang Yang, Lei Chen, Xiaohua Fan, Yunbo Chen, Weiwei Li, Youqiang Fei, Thermal conductivity enhancement of phase change materials with form-stable carbon bonded carbon fiber network, *Mater. Des.* 143 (2018) 177–184.
- [21] Yu Liu, Delong He, Ann-Lenaig Hamon, Benhui Fan, Paul Hagh-Ashtiani, Thomas Reiss, Jinbo Bai, Comparison of different surface treatments of carbon fibers used as reinforcements in epoxy composites: Interfacial strength measurements by in-situ scanning electron microscope tensile tests, *Compos. Sci. Technol.* 167 (2018) 331–338.
- [22] A.A. Stepashkin, D.I. Chukov, M.V. Gorshenkov, V.V. Tcherdyntsev, S.D. Kaloshkin, Electron microscopy investigation of interface between carbon fiber and ultra high molecular weight polyethylene, *J. Alloy. Compd.* 586 (2014) S168–S172.
- [23] Masahito Ueda, Wataru Saito, Ryuma Imahori, Daichi Kanazawa, Tae-Kun Jeong, Longitudinal direct compression test of a single carbon fiber in a scanning electron microscope, *Compos. A Appl. Sci. Manuf.* 67 (2014) 96–101.
- [24] Bradley A. Newcomb, Processing, structure, and properties of carbon fibers, *Compos. A Appl. Sci. Manuf.* 91 (2016) 262–282.
- [25] Bradley A. Newcomb, Lucille A. Giannuzzi, Kevin M. Lyons, Prabhakar V. Gulgunje, Kishor Gupta, Yaodong Liu, Manjeshwar Kamath, et al., High resolution transmission electron microscopy study on polyacrylonitrile/carbon nanotube based carbon fibers and the effect of structure development on the thermal and electrical conductivities, *Carbon* 93 (2015) 502–514.
- [26] Zhenjun Wang, Jie Gao, Tao Ai, Wei Jiang, Peng Zhao, Quantitative evaluation of carbon fiber distribution in cement based composites, *Constr. Build. Mater.* 68 (2014) 26–30.
- [27] Farzad Naseri, Faezeh Jafari, Ehsan Mohseni, Waiching Tang, Abdossattar Feizbakhsh, Mohsen Khatibinia, Experimental observations and SVM-based prediction of properties of polypropylene fibres reinforced self-compacting composites incorporating nano-CuO, *Constr. Build. Mater.* 143 (2017) 589–598.
- [28] L. Shi, S.T.K. Lin, Y. Lu, L. Ye, Y.X. Zhang, Artificial neural network based mechanical and electrical property prediction of engineered cementitious composites, *Constr. Build. Mater.* 174 (2018) 667–674.
- [29] Ke Zhang, Miao Sun, Tony X. Han, Xingfang Yuan, Liru Guo, Tao Liu, Residual networks of residual networks: Multilevel residual networks, *IEEE Trans. Circuits Syst. Video Technol.* 28 (6) (2018) 1303–1314.
- [30] Xi Peng, Lu. Canyi, Zhang Yi, Huajin Tang, Connections between nuclear-norm and frobenius-norm-based representations, *IEEE Trans. Neural Networks Learn. Syst.* 29 (1) (2018) 218–224.
- [31] Ming Yan, Jixiang Guo, Weidong Tian, Zhang Yi, Symmetric convolutional neural network for mandible segmentation, *Knowl.-Based Syst.* 159 (2018) 63–71.
- [32] Long Ang Lim, Hacer Yalim Keles, Foreground segmentation using convolutional neural networks for multiscale feature encoding, *Pattern Recognit. Lett.* 112 (2018) 256–262.
- [33] Zheng Tong, Jie Gao, Haitao Zhang, Recognition, location, measurement, and 3D reconstruction of concealed cracks using convolutional neural networks, *Constr. Build. Mater.* 146 (2017) 775–787.
- [34] Zheng Tong, Jie Gao, Zhenqiang Han, Zhenjun Wang, Recognition of asphalt pavement crack length using deep convolutional neural networks, *Road Mater. Pavement Des.* 19 (6) (2018) 1334–1349.
- [35] Zhenjun Wang, Wu. Jiayu, Peng Zhao, Nan Dai, Zhiwei Zhai, Tao Ai, Improving cracking resistance of cement mortar by thermo-sensitive poly N-isopropyl acrylamide (PNIPAM) gels, *J. Cleaner Prod.* 176 (2018) 1292–1303.
- [36] Hai Liu, Aimin Sha, Zheng Tong, Jie Gao, Autonomous microscopic bunch inspection using region-based deep learning for evaluating graphite powder distribution, *Constr. Build. Mater.* 173 (2018) 525–539.
- [37] Jie Gao, Aimin Sha, Zhenjun Wang, Hu. Lipun, Di Yun, Zhuangzhuang Liu, Yue Huang, Characterization of carbon fiber distribution in cement-based composites by Computed Tomography, *Constr. Build. Mater.* 177 (2018) 134–147.
- [38] Shiliang Pu, Tao Song, Yuan Zhang, Di Xie, Estimation of crowd density in surveillance scenes based on deep convolutional neural network, *Procedia Comput. Sci.* 111 (2017) 154–159.
- [39] T. Ponikiewski, J. Katzer, M. Buggol, M. Rudzki, Determination of 3D porosity in steel fibre reinforced SCC beams using X-ray computed tomography, *Constr. Build. Mater.* 68 (2014) 333–340.
- [40] T. Ponikiewski, J. Katzer, M. Buggol, M. Rudzki, Steel fibre spacing in self-compacting concrete precast walls by X-ray computed tomography, *Mater. Struct.* (2015), <https://doi.org/10.1617/s11527-014-0444-y>.
- [41] T. Ponikiewski, J. Katzer, M. Buggol, M. Rudzki, X-ray computed tomography harnessed to determine 3D spacing of steel fibres in self compacting concrete (SCC) slabs, *Constr. Build. Mater.* 74 (2015) 102–108.

- [42] T. Ponikiewski, J. Katzer, X-ray computed tomography of fibre reinforced self-compacting concrete as a tool of assessing its flexural behaviour, *Mater. Struct.* 49 (6) (2016) 2131–2140, <https://doi.org/10.1617/s11527-015-0638-y>.
- [43] Zheng Tong, Jie Gao, Aimin Sha, Hu Liqun, Shuai Li, Convolutional neural network for asphalt pavement surface texture analysis, *Comput.-Aided Civ. Infrastruct. Eng.* 33 (12) (2018) 1056–1072.
- [44] Zheng Tong, Jie Gao, Haitao Zhang, Innovation for evaluating aggregate angularity based upon 3D convolutional neural network, *Constr. Build. Mater.* 155 (2017) 919–929.
- [45] Holger R. Roth, Lu Le, Amal Farag, Hoo-Chang Shin, Jiamin Liu, Evrim B. Turkbey, Ronald M. Summers, Deeporgan: multi-level deep convolutional networks for automated pancreas segmentation, in: International Conference on Medical Image Computing and Computer-assisted Intervention, Springer, Cham, 2015, pp. 556–564.
- [46] D.D. Chung, Distribution of short fibers in cement, *J. Mater. Civ. Eng.* 17 (4) (2005) 379–383.
- [47] Chuang Wang, Ke-Zhi Li, He-Jun Li, Geng-Sheng Jiao, Lu Jinhua, Dang-She Hou, Effect of carbon fiber distribution on the mechanical properties of carbon fiber-reinforced cement-based composites, *Mater. Sci. Eng., A* 487 (1–2) (2008) 52–57.
- [48] C.A. Juarez, G. Fajardo, S. Monroy, A. Duran-Herrera, P. Valdez, Camille Magniont, Comparative study between natural and PVA fibers to reduce plastic shrinkage cracking in cement-based composite, *Constr. Build. Mater.* 91 (2015) 164–170.